

## Multidimensional Entanglement Generation with Multicore Optical Fibers

E.S. Gómez<sup>1,2,\*</sup>, S. Gómez,<sup>1,2</sup> I. Machuca,<sup>1,2</sup> A. Cabello,<sup>3,4</sup> S. Pádua,<sup>5</sup> S.P. Walborn,<sup>1,2</sup> and G. Lima<sup>1,2</sup>


<sup>1</sup>*Departamento de Física, Universidad de Concepción, Concepción 160-C, Chile*

<sup>2</sup>*ANID—Millennium Science Initiative Program—Millennium Institute for Research in Optics, Universidad de Concepción, Concepción 160-C, Chile*

<sup>3</sup>*Departamento de Física Aplicada II, Universidad de Sevilla, Sevilla E-41012, Spain*

<sup>4</sup>*Instituto Carlos I de Física Teórica y Computacional, Universidad de Sevilla, Sevilla E-41012, Spain*

<sup>5</sup>*Departamento de Física, Universidade Federal de Minas Gerais, Belo Horizonte, Minas Gerais 31270-901, Brazil*

 (Received 31 May 2020; revised 9 November 2020; accepted 3 December 2020; published 9 March 2021)

Trends in photonic quantum information follow closely the technical progress in classical optics and telecommunications. In this regard, advances in multiplexing optical communications channels have also been pursued for the generation of multidimensional quantum states (qudits), since their use is advantageous for several quantum information tasks. One current path leading in this direction is through the use of space-division multiplexing multicore optical fibers, which provides a platform for efficiently controlling path-encoded qudit states. Here, we report on a parametric down-conversion source of entangled qudits that is fully based on (and therefore compatible with) state-of-the-art multicore-fiber technology. The source design uses modern multicore-fiber beam splitters to prepare the pump-laser beam as well as measure the generated entangled state, achieving high spectral brightness while providing a stable architecture. In addition, it can be readily used with any core geometry, which is crucial since widespread standards for multicore fibers in telecommunications have yet to be established. Our source represents a step toward the compatibility of quantum communications with the next-generation optical networks.

DOI: [10.1103/PhysRevApplied.15.034024](https://doi.org/10.1103/PhysRevApplied.15.034024)

### I. INTRODUCTION

In quantum information, there are several protocols that have an improved performance when implemented with multidimensional quantum systems (qudits). For instance, single-qudit states can be exploited for building quantum cryptographic schemes supporting more component imperfections [1], for efficient strategies solving communication complexity problems [2,3], and for advanced phase-estimation algorithms [4,5]. Moreover, multidimensional entanglement allows for two critical advantages related with Bell tests of quantum nonlocality [6], which are the building blocks of entanglement-based quantum information protocols [7]. Specifically, some Bell inequalities for qudits have the property that their genuine quantum violation can still be achieved while working with lower (compared to qubits) overall detection efficiencies [8], which is arguably the main technological challenge of loophole-free Bell experiments. Second, there is a family of Bell inequalities specially tailored for entangled qudits [9,10], the quantum violation of which can still be achieved in a

regime where noisy setups would be regarded as useless if based solely on the famous Clauser-Horne-Shimony-Holt Bell inequality [11,12].

Traditionally, the transverse momentum of single photons has been used for encoding qudit states for over almost two decades now [13–17]. The distribution of photonic quantum states using optical fibers is a fundamental building block toward quantum networks, but due to effects such as decoherence-inducing mode coupling and the limited number of modes supported, the transmission of such spatially encoded qudits over conventional multimode and single-mode fibers has always been considered a formidable challenge. Interesting strategies in this direction have been presented recently [18,19] but they are still limited to the transmission in the range of a few meters for multimode fibers and they are unable to fully exploit the advantages provided by qudits in the case of single-mode fibers (SMFs). Alternatively, there is a new trend emerging for the fiber propagation of spatially encoded qudits that is based on new types of optical fibers developed for space-division multiplexing (SDM) in classical telecommunications [20]. Basically, SDM technology increases data transmission in classical networks by adopting fibers

\*[estesepulveda@udec.cl](mailto:estesepulveda@udec.cl)

capable of simultaneously supporting several transverse optical modes, where the information is then multiplexed [21]. Since the mode coupling in these fibers is minimal, high-fidelity coherent transmission of entangled and single spatially encoded qudits has been already demonstrated up to a few kilometers [22–24].

In this work, we introduce a source of entangled path-encoded qudit states, which is fully based on SDM multicore-fiber (MCF) technology. Multicore fibers have several cores within the same cladding and each core mode can be used to define the logical basis in the path-encoding strategy, as we explain below. Moreover, the relative phase between two different cores of a MCF has been shown to be orders of magnitude more stable than two single-mode fibers [24]. Consequently, these fibers have already been exploited for multidimensional quantum cryptography [25,26], quantum random-number generation [27], quantum computation [5], and Bell inequality violation [28,29]. Path encoding has the significant appeal that  $d$ -dimensional arbitrary operations can be implemented with conventional linear optical elements [30] and this has now become the standard encoding strategy in experiments with integrated photonic circuits [31,32]. Therefore, our source of path entanglement can be used as a resource for the implementation of entanglement-based quantum information protocols in experiments based solely on new MCF technology [27] or also to efficiently distribute multidimensional entanglement between integrated circuits, which are proven to be compatible with MCFs [26]. Our source compares favorably in terms of integrability and brightness with previous works for fiber-based generation of multidimensional path entanglement [28,29,33] and represents a step toward the compatibility of quantum communications with the next-generation SDM optical networks.

## II. QUANTUM INFORMATION WITH MCF TECHNOLOGY

Multicore fiber is currently being pursued for its capability to increase communications rates in telecommunications [21]. At the same time, several authors have investigated MCF technologies in photonic quantum information platforms (for a review, see Ref. [20]). Here, we employ four-core fibers (4CFs). Figure 1(a) shows an image of the facet of a 4CF taken with a standard fiber-inspection microscope and a camera. The cores are approximately  $8\ \mu\text{m}$  wide, corresponding to single mode at  $1550\ \text{nm}$ , arranged on the vertices of a square with  $50\ \mu\text{m}$  sides, which is large enough so that cross-core coupling is greatly reduced. This allows us to treat the spatial modes of each core as independent. For the 4CF, we thus define the path logical basis consisting of the core states  $|j\rangle$ , ( $j = 0, \dots, 3$ ), as also shown in Fig. 1(a).

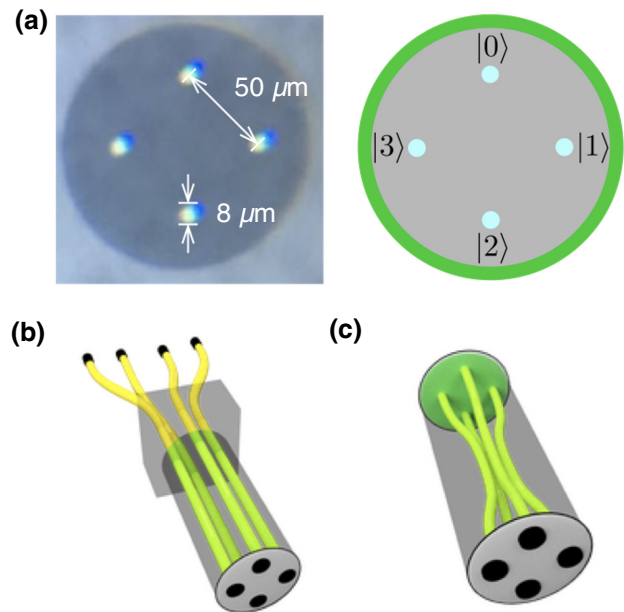


FIG. 1. (a) A photograph of a multicore fiber with four cores (a 4CF) taken with a camera and a fiber microscope (left) and a diagram of the path-encoding strategy for defining the logical states in dimension  $d = 4$  (right). (b) The demultiplexer device, coupling single-mode fibers to a multicore fiber (here, 4CF). (c) A  $4 \times 4$  beam splitter constructed within a 4CF.

In addition to patch cords of MCF, crucial MCF-compatible optical devices have recently been developed that will allow widespread use of MCF technology in photonic quantum information. The first is the demultiplexer (DM) device, as exemplified in Fig. 1(b), which allows one to couple  $N$  single-mode fibers to an  $N$ -core fiber. With this, light can be sent from a standard single-mode fiber into one core of a MCF or vice versa, providing compatibility with standard optical-fiber components. For example, we can couple a photon in mode  $|j\rangle$  of an MCF via a DM to a fiber-ready single-photon detector.

Another notable device is the MCF-based beam splitter (MCF-BS), shown in Fig. 1(c) for a 4CF. The beam splitter is produced by heating and stretching a section of homogeneous MCF (without refractive-index trenches), so that the cores become closer together, enabling evanescent coupling between the cores [34]. The 4CF-BS and a 7CF-BS have been characterized experimentally in Ref. [27]. When the proximity region is small, one can achieve an approximate 25% coupling between all four cores of a 4CF [27]. In the experiment reported here, we use two types of 4CF-BS devices. The first is designed for use at  $775\ \text{nm}$  and the second at  $1550\ \text{nm}$ . More technical details are given below. To a reasonable approximation, the 4CF-BS can be

represented by the unitary matrix

$$U_{\text{BS}} = \frac{1}{2} \begin{bmatrix} 1 & 1 & 1 & 1 \\ 1 & 1 & -1 & -1 \\ 1 & -1 & 1 & -1 \\ 1 & -1 & -1 & 1 \end{bmatrix}. \quad (1)$$

The 4CF-BS thus takes a photon in path state  $|j\rangle$  to an equally weighted superposition state of the form  $|\psi_j\rangle = 1/2 \sum_k u_{kj} |k\rangle$ , where  $u_{kj} = \pm 1$  are the entries of the matrix given in Eq. (1). Likewise, the 4CF-BS can be used to map superposition states into logical basis states:  $U_{\text{BS}} |\psi_j\rangle = |j\rangle$ .

These MCF devices can be connected with relatively low losses (about 2%–5% at 1550 nm) using standard FC/PC fiber connectors [27]. We note that the future development of one more MCF-based optical primitive, namely MCF-integrated phase shifters, will allow for entire multipath optical circuits to be created entirely within multicore fibers. This will allow for the implementation of complex interferometers in a relatively stable MCF platform [24], for use in both quantum and classical optics applications such as communications and metrology. Moreover, multiport beam-splitter devices have recently been shown to provide advantages in quantum logic operations [35,36]. This motivates the development of entangled-photon sources that are compatible with MCF technology.

### III. EXPERIMENT

#### A. Setup

Spontaneous parametric down-conversion (SPDC) is a nonlinear optical process that has traditionally been used to produce correlated photon pairs [37,38]. Here, we use SPDC to construct a source of entangled path qudit states, which is fully based on (and therefore compatible with) state-of-the-art MCF technology. The adopted setup is shown in Fig. 2(a). A fiber-based continuous-wave diode laser operating at 773 nm is used to excite a 1-cm-long type-0 periodically poled lithium niobate (PPLN) crystal, generating down-converted photon pairs at a center wavelength of 1546 nm. The primary goals for the design are for the source to be scalable and to have high spectral brightness and stable performance. The main idea is to coherently illuminate the PPLN crystal in four regions corresponding to the cores of the fiber, following the same core layout as that of the face of the 4CF shown in Fig. 1(a). We note that multipot coherent illumination of nonlinear crystals for the generation of path-entangled photons was presented in the 1990s [39] and has been used frequently since then [29,32,33,40]. However, in our source, the preparation and measurement stages are fully built using SDM optical-fiber technology, aiming for compactness and connectivity with next-generation optical-fiber

networks. To coherently illuminate our PPLN crystal in a robust and efficient way, we take advantage of the developed MCF beam splitters described above [27]. The pump laser is connected to a SMF of the DM and consequently coupled to a single core of the 4CF at its output side. Then, the pump beam is sent through a custom-made 4CF-BS, designed to operate at 775 nm, that coherently splits the pump beam among the four cores of the 4CF. The recorded split ratios of this 4CF-BS are 23.79%, 24.88%, 27.19%, and 24.14% at 773 nm. A fiber polarization controller (PC), placed before the DM, is used to guarantee that the pump polarization can be aligned with the extraordinary axis of the PPLN crystal, to maximize the photon-pair generation rate.

The output face of the 4CF-BS is imaged using the  $2f - 2f'$  imaging configuration onto a plane at the center of the PPLN crystal using lenses  $L_1$  (focal length  $f = 11$  mm) and  $L_2$  ( $f = 50$  mm), arranged confocally, giving an approximately  $4.5\times$  magnified image of the 4CF face. The down-converted pairs are produced at each one of the illuminated regions corresponding to the four fiber cores of the MCF [see the crystal inset of Fig. 2(a)]. The generated photon pairs are then sent through confocal lenses  $L_3$  ( $f = 50$  mm) and  $L_4$  ( $f = 11$  mm) that perform the inverse operation, creating a demagnified image of the down-converted pairs at the face of the output 4CF and coupling them into the fiber. We note that the propagation direction through the crystal should be the same for each core, due to the symmetry of the cores and the design of the imaging system. Moreover, since our PPKTP nonlinear crystal is cut for type-0 SPDC, the down-converted photons have the same polarization and therefore suffer the same walk-off from birefringence. Due to the symmetry of the source, this should also be independent of the core in which the photons are produced. Thus, walk-off should not be an issue and, indeed, we do not observe any noticeable effects. A band-pass and interference filter centered at 1540 nm are used (between the lenses, not shown for sake of clarity) to remove the remaining light from the pump beam.

Considering the split ratio recorded of the 4CF-BS and the fact that it is not possible in principle to distinguish which region of the crystal produces the photon pair, the generated two-photon state can be approximately written as a coherent superposition of the form

$$|\Psi\rangle = \frac{1}{2}(|00\rangle + |11\rangle + |22\rangle + |33\rangle), \quad (2)$$

where we use the shorthand notation  $|jj\rangle = |j\rangle_A \otimes |j\rangle_B$ .

After the source, the down-converted photons are sent to one of two measurement devices shown in Figs. 2(b) and 2(c). In each of these, photon pairs are detected by measuring coincidence counts  $C_{jk}$  ( $j, k = 0, 1, 2, 3$ ), where here  $j$  and  $k$  refer to the core modes of the down-converted

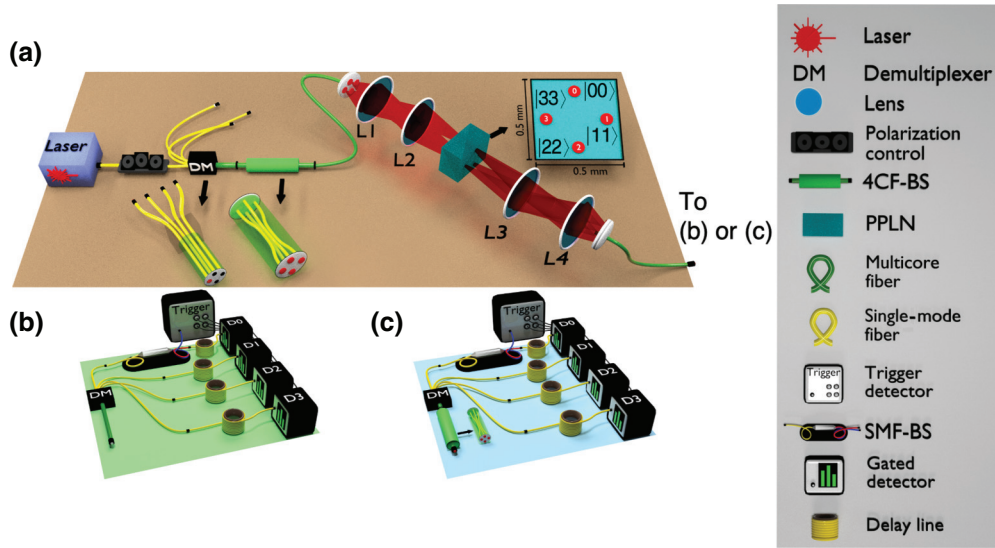


FIG. 2. (a) The schematics of the experimental setup. Entangled qudit states are generated by resorting to coherent illumination of multiple regions of a nonlinear crystal and MCF technology. The generated entangled qudits are sent to one of the detection systems. (b) The detection system for  $Z$  measurements, in which each core of the source output MCF is coupled to a SMF via a demultiplexer DM. Single-photon detectors register coincidences between the photon pairs. (c) The detection system for  $X_j$  basis measurements. In this case, the output of the entanglement source is first coupled to a  $4 \times 4$  MCF-BS and its output fiber is the coupled to SMFs using a DM.

idler and signal photon, respectively. To detect the photons in the path ( $Z$ ) basis, we use the measurement system sketched in Fig. 2(b). The output 4CF of the source is connected to a DM, coupling each core to a SMF. To detect photons propagating over the SMFs a home-made coincidence-count system is used, which works as follows: a free-running trigger single-photon detector (Idquantique ID220) is connected to one of the SMFs, let us say the fiber “0” (associated to core “0”), as shown in Fig. 2(b), using a standard beam splitter (SMF-BS). When it registers a photon, a sync electrical pulse is sent to the four externally gated detectors (Idquantique ID210) for coincidence detections. These detectors are connected to the SMFs using optical delay lines such that coincidence counts can be registered using the sync signal. The ID210 detectors are configured with 25% detection efficiency and 5-ns gate width, while the ID220 detector is configured with 15% detection efficiency and  $5 \mu\text{s}$  of dead time. To observe all of the 16 possible coincidence events  $C_{jk}$ , the ID220 is connected through a SMF-BS to each of the four SMFs and counts of the form  $C_{j0}$ ,  $C_{j1}$ ,  $C_{j2}$ , and  $C_{j3}$  are recorded for all values of  $j$ , with an integration time of 5 s.

For measurements in bases complementary to the  $Z$  basis, we first connect the output 4CF of the source to a 4CF-BS, as shown in Fig. 2(c). The MCF output of the 4CF-BS is then routed through a DM and each core coupled again to the SMFs. The coincidence detection scheme is the same as in Fig. 2(b). Including the relative phases corresponding to propagation in each core, the 4CF-BS

allows us to measure in superposition bases of the form

$$|0\rangle_D = \frac{1}{2} (e^{i\phi_0}|0\rangle + e^{i\phi_1}|1\rangle + e^{i\phi_2}|2\rangle + e^{i\phi_3}|3\rangle), \quad (3a)$$

$$|1\rangle_D = \frac{1}{2} (e^{i\phi_0}|0\rangle + e^{i\phi_1}|1\rangle - e^{i\phi_2}|2\rangle - e^{i\phi_3}|3\rangle), \quad (3b)$$

$$|2\rangle_D = \frac{1}{2} (e^{i\phi_0}|0\rangle - e^{i\phi_1}|1\rangle + e^{i\phi_2}|2\rangle - e^{i\phi_3}|3\rangle), \quad (3c)$$

$$|3\rangle_D = \frac{1}{2} (e^{i\phi_0}|0\rangle - e^{i\phi_1}|1\rangle - e^{i\phi_2}|2\rangle + e^{i\phi_3}|3\rangle), \quad (3d)$$

where  $|j\rangle_D$  refers to the state at detector  $D_j$  after the 4CF-BS and the  $\phi_j$  are the relative phases acquired over core  $j$ . One can switch between four mutually unbiased bases  $X_j$  by choosing different values of the phases  $\phi_j$ . We define the bases as  $X_0 \rightarrow \phi_0 = \phi_1 = \phi_2 = \phi_3 = 0$ ,  $X_1 \rightarrow \phi_0 = 0, \phi_1 = \pi, \phi_2 = \phi_3 = \pi/2$ ,  $X_2 \rightarrow \phi_0 = 0, \phi_1 = \phi_3 = \pi/2, \phi_2 = \pi$ ,  $X_3 \rightarrow \phi_0 = 0, \phi_1 = \phi_2 = \pi/2, \phi_3 = \pi$ . The  $X_j$  bases are mutually unbiased to the  $Z$  basis and also to each other.

## B. Source characterization

Now we describe several characteristics of the source. To ensure the spatially homogeneous generation of down-converted photons over the entire transverse profile of the crystal, we perform a separate experiment in which the 773-nm laser is sent through a single-mode fiber and

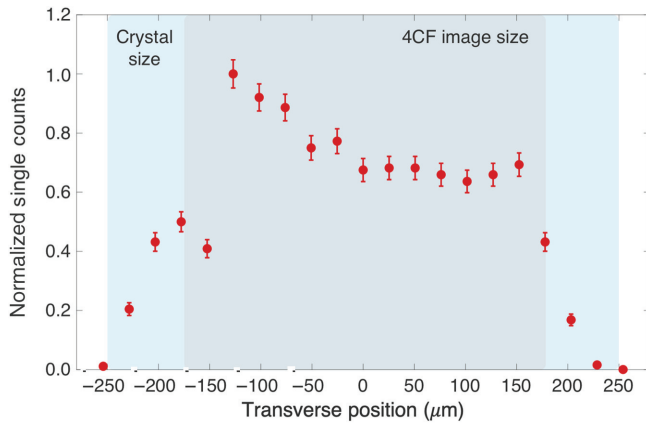


FIG. 3. Normalized single counts while scanning the vertical ( $y$ -axis) transverse direction of the PPLN crystal, recorded by a pointlike single-photon detector. The shaded regions correspond to the dimensions of the crystal and the image size of the 4CF.

used to illuminate the center of the crystal through the imaging system composed by lenses  $L_1$  and  $L_2$ . The down-converted light is coupled into a pointlike detector, composed of another single-mode fiber for 1550 nm connected directly to an ID210 detector. We scan the crystal along the (transverse) horizontal ( $x$ ) and vertical ( $y$ ) axes, recording the corresponding detector single counts. As an example, Fig. 3 shows the spatial distribution of the down-converted photons with the crystal scanned in the  $y$  direction. Similar results are obtained for the  $x$  direction. We recognize an approximately 380- $\mu\text{m}$ -wide region where the photons can be created. Considering the core size and the separation between them, we choose a magnification factor of 4.5 such that the image size of the 4CF at the PPLN crystal is approximately 350  $\mu\text{m}$ . In this way, the crystal generates photon pairs in the four different illuminated regions defined by the image of the 4CF.

Further, since quasi-phase-matching conditions are achieved by adjusting the temperature of the crystal, we test that the optimal temperature is the same for each of the regions corresponding to the four cores. We adjust the PPLN crystal temperature by placing it in an electronically controlled oven. Figure 4 shows the normalized coincidence counts in each core, as a function of the temperature, recorded using the measurement scheme of Fig. 2(b). We observe that at 112  $^{\circ}\text{C}$ , a nearly optimized coincidence rate of SPDC in all cores is reached, in correspondence with the pump and down-converted photon wavelengths and the crystal poling period (19.8  $\mu\text{m}$ ). Moreover, the fact that the four regions produce intensity peaks centered at the same temperature indicates that the frequency light spectra from each core are similar, since the interference filter selects photons near 1540 nm for all cores.

The brightness of the source is a notable characteristic, if entanglement is to be distributed over long-distances through optical fibers. Our entanglement source operates

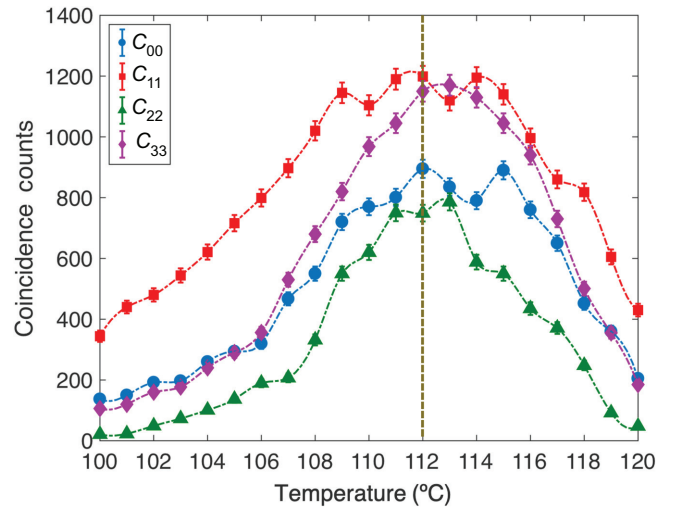


FIG. 4. The coincidence rate in each independently illuminated core as a function of the crystal temperature. The optimal temperature to satisfy the phase-matching conditions for all cores is 112  $^{\circ}\text{C}$ .

with a pump-laser power of 1 mW per core. Taking this into account, plus the insertion losses of the optical devices and detector efficiencies (approximately 4% in coincidence), the observed spectral brightness of the source is approximately 350 000 photon pairs  $(\text{s mW nm})^{-1}$ , which is comparable with optimized sources for polarization entangled photons [41]. Considering the typical loss in multicore optical fibers of 0.4 dB per km for 1550 nm, it would be possible to distribute multidimensional entanglement over at least approximately 75 km of fiber. Thus, this source can be readily employed to investigate the propagation of spatial entanglement over long multicore fibers, which has yet to be realized.

Another notable feature of our source is the phase stability provided by coupling the pump and the down-converted light directly in and out of 4CFs, which are inherently robust against thermal fluctuations and mechanical stress since the cores lie within the same cladding [24,25]. The relative phase between two different cores of a MCF can be at least 2 orders of magnitude more stable than two single-mode fibers over a 2-km length [24]. When the  $X_j$  measurement bases are implemented, the last 4CF-BS combines together the incoming down-converted photons, forming an interferometer that is sensitive to phase fluctuations. Due to the stability of the 4CF, without any fiber-isolation system or active-phase stabilization, we observe that phase oscillations typically occur with a period of several minutes. To test this, we record coincidence measurements for more than 10 min. We then perform a Fourier analysis of the coincidence counts recorded over time, which reveals the relevant frequency components. Figure 5 shows the absolute value of the frequency spectrum for sample coincidence measurements recorded at different times. The peaks of these distributions correspond to oscillations with

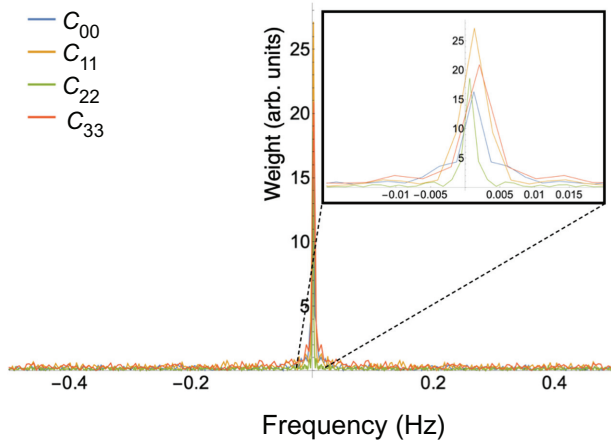


FIG. 5. The spectrum of frequency components of the coincidence counts between different detectors using the detection system shown in Fig. 2(c), taken at different times. Fluctuations due to phase changes occur on a time scale of several minutes.

a period between 2 and 6.5 min. We can see that there are essentially no frequencies components larger than 0.008 Hz, meaning that the interferometer is stable on the scale of a few minutes. Our goal here is to present the fundamental characteristics of the source but we note that, if necessary, one can employ the technique of Ref. [27] to phase lock the source.

### C. Entanglement certification

We measure coincidence counts  $C_{jk}$  as explained in Sec. III A. Accidental coincidence counts  $a_{jk}$  arising from dark counts and ambient light are evaluated by recording the average count rate with a large relative electronic delay between detectors. The corrected coincidence counts, given by  $C_{jk}^c = C_{jk} - a_{jk}$ , are used to estimate the joint probability distributions:  $P_{jk} = C_{jk}^c / \sum_{jk} C_{jk}^c$ . The experimental error is calculated by assuming Poissonian count statistics and Gaussian error propagation. The recorded probability distributions while measuring both photons in the Z basis is shown in Fig. 6(a), with photons always found in the same core.

For measurements in the  $X_j$  bases, there are two-photon coalescence effects on the 4CF-BS that impose a convenient symmetry to the coincidence counts. By considering the state of Eq. (2) and the measurements of Eqs. (3), we see that the coincidence-count probabilities at detectors  $j$  and  $k$  ( $j, k = 0, 1, 2, 3$ ) are given by

$$P_{jk}^{the} = \left| \frac{1}{8} \sum_{m=0}^3 u_{mj} u_{mk} e^{i2\phi_m} \right|^2, \quad (4)$$

where  $u_{mj}, u_{mk} = \pm 1$  are the sign of the entries in the matrix given in Eq. (1). In this case, when the relative phases are such that complete constructive and/or

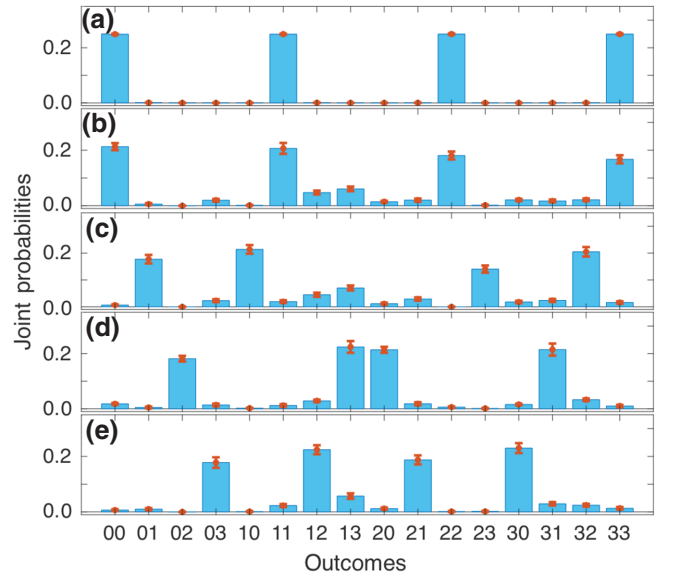


FIG. 6. The joint probability distributions obtained while measuring both photons in the (a) Z basis, (b)  $X_0$  basis, (c)  $X_1$  basis, (d)  $X_2$  basis, and (e)  $X_3$  basis. The error bars are obtained considering Gaussian error propagation and Poissonian photocount statistics.

destructive interference occurs, only four of the 16 probabilities  $P_{mn}$  are nonzero. For example, when all of the phases are equal, the four probabilities  $P_{00} = P_{11} = P_{22} = P_{33} = 1/4$ . Since these four probabilities sum to one, all the rest are zero. This case corresponds to detection of both photons in the  $X_0$  basis. For the phases corresponding to the  $X_1$  basis, only probabilities  $P_{01} = P_{10} = P_{23} = P_{31} = 1/4$  are nonzero. Likewise, for the  $X_2$  basis, we have  $P_{02} = P_{20} = P_{13} = P_{31} = 1/4$  and all others equal to zero, while for  $X_3$  we have  $P_{03} = P_{30} = P_{12} = P_{21} = 1/4$  with the rest equal to zero. In this fashion, observing a maximum in one coincidence-count group while observing all of the others near zero allows us to identify the relative phase values.

The measurements in the  $X_i$  bases are identified using the coincidence-count signatures described above, while applying a controlled bending to the 4CF fiber at the output of the source, causing mechanical stress that changes the relative phases between cores [42]. The joint probability distributions obtained from the four  $X_i$  measurements are shown in Fig. 6. The similarity,  $C_B$ , of the recorded and theoretical probability distributions can be quantified using the Bhattacharyya coefficient [43]. In our case, it reaches  $C_B = 0.91 \pm 0.02$ , showing good agreement between theory and experiment. The unwanted nonzero terms in Figs. 6(b)–6(e) arise due to phase fluctuations as well as imprecision in setting the relative phases between the four cores. We use the dependence of the phase on the bend and orientation of the optical fiber to adjust the phase, which though not very precise, is sufficient to adjust the four complementary coincidence signatures. The

more relevant issue is that of phase instability. Though the interferometer is quite stable, as shown in Fig. 5, there can still be some slight phase variation over the measurement acquisition time (20 s), which reduces the interference visibility. The phase instability results in a slight dephasing of the state, which is reflected in the nonzero probability elements and reduces the fidelity with the ideal state. Both of these phase errors can be reduced by constructing active phase control, which at present requires removing the light from the MCF and into single-mode fiber phase modulators, which is undesirable. We note that this is completely feasible and has been done in Ref. [27].

### 1. Fidelity

To certify the multidimensional entanglement of the generated state  $\rho$ , we use its fidelity  $F(\rho, |\Psi\rangle) = \langle \Psi | \rho | \Psi \rangle$  to the target state  $|\Psi\rangle$  in Eq. (2). Explicitly,

$$F(\rho, |\Psi\rangle) = \sum_{j=0}^3 \langle jj | \rho | jj \rangle + 2 \sum_{\substack{j=0 \\ k=j+1}}^3 \text{Re}[\langle jj | \rho | kk \rangle]. \quad (5)$$

The first term can be obtained directly from the measurements in the  $Z$  basis, where we have  $P_{jj} = \langle jj | \rho | jj \rangle$ . The second term corresponds to the coherence between states  $|jj\rangle$  and  $|kk\rangle$ . These can be calculated by defining Pauli operators for the  $j, k$  subspace as follows [44,45]:  $\sigma_x^{(jk)} = |j\rangle\langle k| + |k\rangle\langle j|$ ,  $\sigma_y^{(jk)} = i|j\rangle\langle k| - i|k\rangle\langle j|$ . Then,  $\text{Re}[\langle jj | \rho | kk \rangle] = ((\sigma_x^{(jk)} \otimes \sigma_x^{(jk)}) - \langle \sigma_y^{(jk)} \otimes \sigma_y^{(jk)} \rangle)/4$ . These expectation values can be evaluated directly from the  $X_i$  measurements, as we describe in detail in the Appendix. Using the recorded data of the five mutually unbiased measurements, we obtain  $F = 0.789 \pm 0.007$ . Since any state with  $F(\rho, |\Psi\rangle) > 3/4$  is incompatible with a Schmidt number  $\leq 3$  [44,45], we can confirm the four-dimensional nature of the entanglement produced by the source.

### 2. High-dimensional steering

Another interesting approach to certify multilevel entanglement generation is that based on quantum steering [46], which is a distinct correlation that lies between entanglement and Bell nonlocality and has been related to one-sided device independent quantum cryptography [47] as well as one-sided device independent randomness generation [48–51]. For two mutually unbiased bases corresponding to observables  $\hat{P}$  and  $\hat{Q}$ , quantum steering can be identified using the entropic criterion [52]

$$S_{JK}^{(PQ)} = H(P_J|P_K) + H(Q_J|Q_K) - \log_2 D \geq 0, \quad (6)$$

where the  $J, K = A, B$  ( $J \neq K$ ) denote the subsystems.  $H(P_J|Q_K)$  is the conditional Shannon entropy calculated over the joint probabilities associated to measurements in

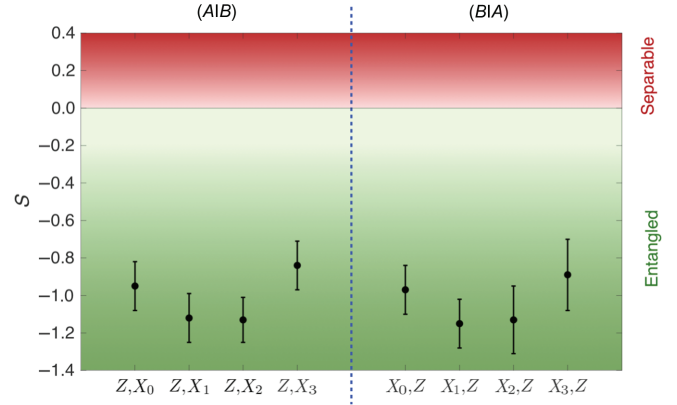


FIG. 7. The experimental values for the EPR-steering criterion  $S$  for steering from  $A$  to  $B$ , denoted  $(B|A)$  and from  $B$  to  $A$ , denoted  $(A|B)$ . When  $S_{JK}^{(PQ)} < 0$ , we can confirm that the state is entangled in the one-sided device independent scenario.

the  $P$  and  $Q$  bases on subsystems  $J$  and  $K$ , respectively. Steering can be an asymmetrical correlation and violation of inequality Eq. (6) indicates steering from subsystem  $K$  to subsystem  $J$  when  $S_{JK}^{(PQ)} < 0$ , which also indicates that the two systems are entangled. Identifying  $P = Z$  and  $Q = X_j$ , we apply these inequalities to our experimentally obtained probabilities of Fig. 6. The conditional entropy is calculated using  $H(P_J|Q_K) = H(P_J, Q_K) - H(Q_K)$ , where  $H(P_J, Q_K)$  is the joint Shannon entropy and  $H(Q_K)$  is the marginal entropy corresponding to local measurement  $Q$  on party  $K$ . The results are shown in Fig. 7. We obtain negative values for all correlations tested, showing that the generated qudit state exhibits steering from  $A$  to  $B$  as well as from  $B$  to  $A$ . We obtain mean values  $\bar{S}_{AB} = -1.01 \pm 0.06$  and  $\bar{S}_{BA} = -1.04 \pm 0.08$ . Identification of steering allows us to confirm that the generated state is entangled in a one-sided device independent scenario [53], meaning that full knowledge of the inner workings of one of the system's devices is not necessary. Moreover, the dimensionality of each subsystem can be observed through the Shannon entropies  $H(P_J)$  and  $H(Q_J)$  of the marginal distributions, which are all very close to the maximum value of  $\log_2 D = 2$  bits for a  $D = 4$  dimensional subsystem. The mean value is  $1.99 \pm 0.02$  bits, which is twice the limit of qubit subsystems.

## IV. CONCLUSION

In this work, we present a design of a source of multidimensional photonic entanglement that is based on SDM optical fibers, thus being fully compatible with next-generation telecommunications fiber networks. The source uses state-of-the-art multicore-fiber technology to illuminate a nonlinear crystal and to measure the generated down-converted photons [27]. The design is flexible, since it allows for the core geometry of the fibers to be changed without realignment of the source, a crucial feature since

MCF technology is in a rapid stage of development and widespread standards have yet to be established. To demonstrate its viability, we prepare an entangled state of two four-dimensional systems, encoded in the path degree of freedom of the down-converted photons, and certify the multidimensional entanglement generation. In addition, quantum steering is identified, indicating entanglement in a one-sided device-independent scenario.

The source presents several technical advantages, including high spectral brightness—comparable with that of modern polarization-entangled-qubit sources—and relatively long phase stability, due to the use of multicore fibers. Consequently, our scheme has several potential applications. For instance, one can exploit the verified multidimensional steering for implementing one-side device-independent quantum protocols such as quantum cryptography or quantum randomness generation [47–51]. The spectral brightness achieved, of 350 000 photon pairs generated  $(\text{s mW nm})^{-1}$ , will allow for future investigations demonstrating the viability of long-distance distribution of multidimensional entanglement over multicore fibers. Finally, we note that the presented scheme is readily available for use in quantum enhanced metrology beyond the standard quantum limit. In particular, the entangled state produced by our source is nearly optimal for multiparameter phase estimation [54].

#### ACKNOWLEDGMENTS

We thank T. García and J. Cariñe for laboratory assistance and M. Huber and G. Xavier for providing valuable comments. This work was supported by the Fondo Nacional de Desarrollo Científico y Tecnológico

(FONDECYT) (Grants No. 1190901, No. 1200266, and No. 1200859) and the National Agency of Research and Development (ANID) Millennium Science Initiative Program—ICN17\_012. S.G. acknowledges ANID. A.C. was supported by the Universidad de Sevilla Project “Quantum Device-Independent Secure Communication over Metropolitan Distances” (Qdisc) (Project No. US-15097), with European Regional Development Fund (FEDER) funds, the Ministry of Economy and Competitiveness (MINECO) Project No. FIS2017-89609-P, with FEDER funds, and the QuantERA grant “SECuRe quantum communication based on Energy-Time/time-bin entanglement” (SECRET), by MINECO (Project No. PCI2019-111885-2). S.P. thanks the Conselho Nacional de Desenvolvimento Científico e Tecnológico (CNPq) and the Instituto Nacional de Ciência e Tecnologia de Informação Quântica (INCT-IQ). S.P. thanks the Departamento de Física of the Universidad de Concepción for the hospitality during his four months of sabbatical leave.

#### APPENDIX: FIDELITY CALCULATION FROM PROBABILITY DISTRIBUTIONS

The fidelity is calculated from the experimental data by defining the Pauli operators for the  $j, k$  subspace as [44,45]:  $\sigma_x^{(jk)} = |j\rangle\langle k| + |k\rangle\langle j|$ ,  $\sigma_y^{(jk)} = i|j\rangle\langle k| - i|k\rangle\langle j|$ . Then,  $\text{Re}[\langle jj|\rho|kk\rangle] = (\langle\sigma_x^{(jk)}\otimes\sigma_x^{(jk)}\rangle - \langle\sigma_y^{(jk)}\otimes\sigma_y^{(jk)}\rangle)/4$ . Let us denote the probabilities from the  $X_j$  measurements as  $P^{(j)} = \{P_{xy}^{(j)}\}$ , with  $x, y = 0, \dots, 3$ . We also define the correlation functions

$$C_j(\alpha, \beta, \gamma, \delta) = [P_{\alpha\alpha}^{(j)} + P_{\alpha\beta}^{(j)} + P_{\beta\alpha}^{(j)} + P_{\beta\beta}^{(j)} + P_{\gamma\gamma}^{(j)} + P_{\gamma\delta}^{(j)} + P_{\delta\gamma}^{(j)} + P_{\delta\delta}^{(j)} - P_{\alpha\gamma}^{(j)} - P_{\alpha\delta}^{(j)} - P_{\alpha\gamma}^{(j)} - P_{\alpha\delta}^{(j)} - P_{\gamma\beta}^{(j)} - P_{\gamma\delta}^{(j)} - P_{\delta\beta}^{(j)} - P_{\delta\gamma}^{(j)}], \quad (\text{A1})$$

for  $\alpha, \beta, \gamma, \delta = 0, 1, 2, 3$ . Then, it is a straightforward but lengthy calculation to show that we can use the  $X_j$  measurement probability distributions in the above correlation function to determine the terms in the Fidelity. Explicitly, we have

$$2\text{Re}[\langle 00|\rho|11\rangle] + 2\text{Re}[\langle 22|\rho|33\rangle] = \frac{1}{4}[C_0(0, 1, 2, 3) + C_1(0, 1, 2, 3) - C_2(0, 1, 2, 3) - C_3(0, 1, 2, 3)], \quad (\text{A2})$$

$$2\text{Re}[\langle 00|\rho|22\rangle] + 2\text{Re}[\langle 11|\rho|33\rangle] = \frac{1}{4}[C_0(0, 2, 1, 3) + C_1(0, 2, 1, 3) - C_2(0, 2, 1, 3) - C_3(0, 2, 1, 3)], \quad (\text{A3})$$

$$2\text{Re}[\langle 00|\rho|33\rangle] + 2\text{Re}[\langle 11|\rho|22\rangle] = \frac{1}{4}[C_0(0, 3, 1, 2) + C_3(0, 3, 1, 2) - C_1(0, 3, 1, 2) - C_2(0, 3, 1, 2)]. \quad (\text{A4})$$



These expressions can be used directly in Eq. (5) to calculate the fidelity.

- 
- [1] N. J. Cerf, M. Bourennane, A. Karlsson, and N. Gisin, Security of Quantum Key Distribution Using  $d$ -Level Systems, *Phys. Rev. Lett.* **88**, 127902 (2002).
- [2] A. Tavakoli and M. Żukowski, Higher-dimensional communication complexity problems: Classical protocols versus quantum ones based on Bell's theorem or prepare-transmit-measure schemes, *Phys. Rev. A* **95**, 042305 (2017).
- [3] D. Martínez, A. Tavakoli, M. Casanova, G. Cañas, B. Marques, and G. Lima, High-Dimensional Quantum Communication Complexity beyond Strategies Based on Bell's Theorem, *Phys. Rev. Lett.* **121**, 150504 (2018).
- [4] M. Araújo, F. Costa, and Č. Brukner, Computational Advantage from Quantum-Controlled Ordering of Gates, *Phys. Rev. Lett.* **113**, 250402 (2014).
- [5] M. M. Taddei, J. Cariñe, D. Martínez, T. García, N. Guerrero, A. A. Abbott, M. Araújo, C. Branciard, E. S. Gómez, S. P. Walborn, L. Aolita, and G. Lima, Experimental computational advantage from superposition of multiple temporal orders of quantum gates, [arXiv:2002.07817](https://arxiv.org/abs/2002.07817) (2020).
- [6] J. S. Bell, On the Einstein Podolsky Rose paradox, *Physics* (College Park, MD) **1**, 195 (1964).
- [7] N. Brunner, D. Cavalcanti, S. Pironio, V. Scarani, and S. Wehner, Bell nonlocality, *Rev. Mod. Phys.* **86**, 419 (2014).
- [8] T. Vértesi, S. Pironio, and N. Brunner, Closing the Detection Loophole in Bell Experiments Using Qudits, *Phys. Rev. Lett.* **104**, 060401 (2010).
- [9] D. Kaszlikowski, P. Gnacinski, M. Żukowski, W. Miklaszewski, and A. Zeilinger, Violations of Local Realism by Two Entangled  $N$ -Dimensional Systems Are Stronger than for Two Qubits, *Phys. Rev. Lett.* **85**, 4418 (2000).
- [10] D. Collins, N. Gisin, N. Linden, S. Massar, and S. Popescu, Bell Inequalities for Arbitrarily High-Dimensional Systems, *Phys. Rev. Lett.* **88**, 040404 (2002).
- [11] J. F. Clauser, M. A. Horne, A. Shimony, and R. A. Holt, Proposed Experiment to Test Separable Hidden-Variable Theories, *Phys. Rev. Lett. A* **23**, 880 (1969).
- [12] J. F. Clauser and M. A. Horne, Experimental consequences of objective local theories, *Phys. Rev. D* **10**, 526 (1974).
- [13] J. Leach, M. J. Padgett, S. M. Barnett, S. Franke-Arnold, and J. Courtial, Measuring the Orbital Angular Momentum of a Single Photon, *Phys. Rev. Lett.* **88**, 257901 (2002).
- [14] A. Vaziri, G. Weihs, and A. Zeilinger, Experimental Two-Photon, Three-Dimensional Entanglement for Quantum Communication, *Phys. Rev. Lett.* **89**, 240401 (2002).
- [15] L. Neves, G. Lima, J. G. Aguirre Gómez, C. H. Monken, C. Saavedra, and S. Pádua, Generation of Entangled States of Qudits Using Twin Photons, *Phys. Rev. Lett.* **94**, 100501 (2005).
- [16] M. N. O'Sullivan-Hale, I. A. Khan, R. W. Boyd, and J. C. Howell, Pixel Entanglement: Experimental Realization of Optically Entangled  $d = 3$  and  $d = 6$  Qudits, *Phys. Rev. Lett.* **94**, 220501 (2005).
- [17] S. P. Walborn, D. S. Lemelle, M. P. Almeida, and P. H. Souto Ribeiro, Quantum key Distribution with Higher-Order Alphabets Using Spatially Encoded Qudits, *Phys. Rev. Lett.* **96**, 090501 (2006).
- [18] N. H. Valencia, S. Goel, W. McCutcheon, H. Defienne, and M. Malik, Unscrambling Entanglement through a Complex Medium, [arXiv:1910.04490](https://arxiv.org/abs/1910.04490) (2019).
- [19] J. Liu, I. Nape, Q. Wang, A. Vallés, J. Wang, and A. Forbes, Multidimensional entanglement transport through single-mode fiber, *Sci. Adv.* **6**, eaay0837 (2020).
- [20] G. B. Xavier and G. Lima, Quantum information processing with space-division multiplexing optical fibres, *Commun. Phys.* **3**, 9 (2020).
- [21] D. J. Richardson, J. M. Fini, and L. E. Nelson, Space-division multiplexing in optical fibres, *Nat. Photonics* **7**, 354 (2013).
- [22] D. Cozzolino, D. Bacco, B. Da Lio, K. Ingerslev, Y. Ding, K. Dalgaard, P. Kristensen, M. Galili, K. Rottwitt, S. Ramachandran, and L. K. Oxenlowe, Orbital Angular Momentum States Enabling Fiber-Based High-Dimensional Quantum Communication, *Phys. Rev. Appl.* **11**, 064058 (2019).
- [23] H. Cao, S.-C. Gao, C. Zhang, J. Wang, D.-Y. He, B.-H. Liu, Z.-W. Zhou, Y.-J. Chen, Z.-H. Li, S.-Y. Yu, J. Romero, Y.-F. Huang, C.-F. Li, and G.-C. Guo, Distribution of high-dimensional orbital angular momentum entanglement over a 1 km few-mode fiber, *Optica* **7**, 232-237 (2020).
- [24] B. Da Lio, L. K. Oxenlowe, D. Bacco, D. Cozzolino, N. Biagi, T. N. Arge, E. Larsen, K. Rottwitt, Y. Ding, and A. Zavatta, Stable transmission of high-dimensional quantum states over a 2-km multicore fiber, *IEEE J. Sel. Top. Quantum Electron.* **26**, 6400108 (2020).
- [25] G. Cañas, N. Vera, J. Cariñe, P. González, J. Cardenas, P. W. R. Connolly, A. Przysieszna, E. S. Gómez, M. Figueroa, G. Vallone, P. Villoresi, T. F. da Silva, G. B. Xavier, and G. Lima, High-dimensional decoy-state quantum key distribution over multicore telecommunication fibers, *Phys. Rev. A* **96**, 022317 (2017).
- [26] Y. Ding, D. Bacco, K. Dalgaard, X. Cai, X. Zhou, K. Rottwitt, and L. K. Oxenlowe, High-dimensional quantum key distribution based on multicore fiber using silicon photonic integrated circuits, *Quantum Inf.* **3**, 25 (2017).
- [27] J. Cariñe, G. Cañas, P. Skrzypczyk, I. Supic, N. Guerrero, T. García, L. Pereira, M. Solís Prosser, G. Xavier, A. Delgado, S. Walborn, D. Cavalcanti, and G. Lima, Multi-port beamsplitters based on multi-core optical fibers for high-dimensional quantum information, *Optica* **7**, 542 (2020).
- [28] H. J. Lee, S. K. Choi, and H. S. Park, Experimental demonstration of four-dimensional photonic spatial entanglement between multi-core optical fibres, *Sci. Rep.* **7**, 4302 (2017).
- [29] H. J. Lee and H. S. Park, Generation and measurement of arbitrary four-dimensional spatial entanglement between photons in multicore fibers, *Photonics Res.* **7**, 19 (2019).
- [30] M. Reck, A. Zeilinger, H. J. Bernstein, and P. Bertani, Experimental Realization of Any Discrete Unitary Operator, *Phys. Rev. Lett.* **73**, 58 (1994).
- [31] J. Carolan, C. Harrold, C. Sparrow, E. Martín López, N. J. Russell, J. W. Silverstone, P. J. Shadbolt, N. Matsuda, M. Oguma, M. Itoh, G. D. Marshall, M. G. Thompson, J. C. F. Matthews, T. Hashimoto, J. L. O'Brien, and A. Laing, Universal linear optics, *Science* **349**, 6249 (2015).

- [32] J. Wang, S. Paesani, Y. Ding, R. Santagati, P. Skrzypczyk, A. Salavrakos, J. Tura, R. Augusiak, L. Mančinska, D. Bacco, D. Bonneau, J. W. Silverstone, Q. Gong, A. Acín, K. Rottwitt, L. K. Oxenlowe, J. L. O'Brien, A. Laing, and M. G. Thompson, Multidimensional quantum entanglement with large-scale integrated optics, *Science* **360**, 285 (2018).
- [33] C. Schaeff, R. Polster, R. Lapkiewicz, R. Fickler, S. Ramelow, and A. Zeilinger, Scalable fiber integrated source for higher-dimensional path-entangled photonic quNits, *Opt. Express* **20**, 16145 (2012).
- [34] L. Gan, R. Wang, D. Liu, L. Duan, S. Liu, S. Fu, B. Li, Z. Feng, H. Wei, W. Tong, P. Shum, and M. Tang, Spatial-division multiplexed Mach-Zehnder interferometers in heterogeneous multicore fiber for multiparameter measurement, *IEEE Photonics J.* **8**, 7800908 (2016).
- [35] M. Y. Saygin, I. V. Kondratyev, I. V. Dyakonov, S. A. Mironov, S. S. Straupe, and S. P. Kulik, Robust Architecture for Programmable Universal Unitaries, *Phys. Rev. Lett.* **124**, 010501 (2020).
- [36] L. Pereira, A. Rojas, G. Cañas, G. Lima, A. Delgado, and A. Cabello, Universal multi-port interferometers with minimal optical depth, [arXiv:2002.01371](https://arxiv.org/abs/2002.01371) (2020).
- [37] D. N. Klyshko, Scattering of light in a medium with nonlinear polarizability, *Sov. Phys. JETP* **28**, 522 (1969).
- [38] D. C. Burnham and D. L. Weinberg, Observation of Simultaneity in Parametric Production of Optical Photon Pairs, *Phys. Rev. Lett.* **25**, 84 (1970).
- [39] A. V. Burlakov, M. V. Chekhova, D. N. Klyshko, S. P. Kulik, A. N. Penin, Y. H. Shih, and D. V. Strekalov, Interference effects in spontaneous two-photon parametric scattering from two macroscopic regions, *Phys. Rev. A* **56**, 3214 (1997).
- [40] X.-M. Hu, W.-B. Xing, B.-H. Liu, Y.-F. Huang, C.-F. Li, G.-C. Guo, P. Erker, and M. Huber, Efficient generation of high-dimensional entanglement through multi-path downconversion, [arXiv:2004.09964](https://arxiv.org/abs/2004.09964) (2020).
- [41] E. S. Gómez, S. Gómez, P. González, G. Cañas, J. F. Barra, A. Delgado, G. B. Xavier, A. Cabello, M. Kleinmann, T. Vértesi, and G. Lima, Device-Independent Certification of a Nonprojective Qubit Measurement, *Phys. Rev. Lett.* **117**, 260401 (2016).
- [42] S. Garcia, M. Urena, and I. Gasulla, Bending and twisting effects on multicore fiber differential group delay, *Opt. Express* **27**, 31290 (2019).
- [43] A. Bhattacharyya, On a measure of divergence between two statistical populations defined by their probability distributions, *Bull. Calcutta Math. Soc.* **35**, 99 (1943).
- [44] A. J. Gutiérrez-Esparza, W. M. Pimenta, B. Marques, A. A. Matoso, J. Sperling, W. Vogel, and S. Pádua, Detection of nonlocal superpositions, *Phys. Rev. A* **90**, 032328 (2014).
- [45] J. Bavaresco, N. Herrera Valencia, C. Klöckl, M. Pivoluska, P. Erker, N. Friis, M. Malik, and M. Huber, Measurements in two bases are sufficient for certifying high-dimensional entanglement, *Nat. Phys.* **14**, 1032 (2018).
- [46] H. M. Wiseman, S. J. Jones, and A. C. Doherty, Steering, Entanglement, Nonlocality, and the Einstein-Podolsky-Rosen Paradox, *Phys. Rev. Lett.* **98**, 140402 (2007).
- [47] C. Branciard, E. G. Cavalcanti, S. P. Walborn, V. Scarani, and H. M. Wiseman, One-sided device-independent quantum key distribution: Security, feasibility, and the connection with steering, *Phys. Rev. A* **85**, 010301(R) (2012).
- [48] Y. Z. Law, L. P. Thinh, J. D. Bancal, and V. Scarani, Quantum randomness extraction for various levels of characterization of the devices, *J. Phys. A Math. Theor.* **47**, 424028 (2014).
- [49] E. Passaro, D. Cavalcanti, P. Skrzypczyk, and A. Acín, Optimal randomness certification in the quantum steering and prepare-and-measure scenarios, *New J. Phys.* **17**, 113010 (2015).
- [50] A. Máttar, P. Skrzypczyk, G. H. Aguilar, R. V. Nery, P. H. S. Ribeiro, S. P. Walborn, and D. Cavalcanti, Experimental multipartite entanglement and randomness certification of the W state in the quantum steering scenario, *Quantum Sci. Technol.* **2**, 015011 (2017).
- [51] S. Gómez, A. Mattar, E. S. Gómez, D. Cavalcanti, O. J. Fariás, A. Acín, and G. Lima, Experimental nonlocality-based randomness generation with nonprojective measurements, *Phys. Rev. A* **97**, 040102(R) (2018).
- [52] J. Schneeloch, C. J. Broadbent, S. P. Walborn, E. G. Cavalcanti, and J. C. Howell, Einstein-Podolsky-Rosen steering inequalities from entropic uncertainty relations, *Phys. Rev. A* **87**, 062103 (2013).
- [53] D. Cavalcanti, P. Skrzypczyk, G. H. Aguilar, R. V. Nery, P. H. S. Ribeiro, and S. P. Walborn, Detection of entanglement in asymmetric quantum networks and multipartite quantum steering, *Nat. Commun.* **6**, 7941 (2015).
- [54] M. A. Ciampini, N. Spagnolo, C. Vitelli, L. Pezzè, A. Smerzi, and F. Sciarrino, Quantum-enhanced multiparameter estimation in multiarm interferometers, *Sci. Rep.* **6**, 28881 (2016).